Photoinduced insulator-to-metal transition and surface statistics of VO_2 monitored by elastic light scattering

Sergiy Lysenko,[1,*] Felix Fernández,[1] Armando Rúa,[1] Nelson Sepúlveda,[2] and Joaquin Aparicio[3]

[1]Department of Physics, University of Puerto Rico, Mayaguez, Puerto Rico 00681, USA

[2]Department of Electrical and Computer Engineering, Michigan State University, East Lansing, Michigan 48824, USA

[3]Department of Physics, University of Puerto Rico-Ponce, Ponce, Puerto Rico 00732, USA

*Corresponding author: sergiy.lysenko@upr.edu

Received 6 October 2014; revised 2 December 2014; accepted 5 December 2014;
posted 23 December 2014 (Doc. ID 223983); published 10 March 2015

Measurements of ultrafast light scattering within a hemisphere are performed for statistical analysis of nonequilibrium processes in VO_2 epitaxial film. A Gerchberg–Saxton error reduction algorithm is applied for accurate calculation of a surface autocorrelation function from light scattering data and for partial reconstruction of a power spectral density function. Upon ultrafast photoinduced phase transition of VO_2, the elastic light scattering reveals anisotropic grain-size-dependent dynamics. It was found that the transition rate depends on the optical absorption and orientation of VO_2 grains with respect to polarization of the pump pulse. An observed stepwise evolution of surface autocorrelation length and transient anisotropy of the scattering field presumably originates from complex multistage transformation of VO_2 lattice on a subpicosecond time scale.

OCIS codes: (320.7130) Ultrafast processes in condensed matter, including semiconductors; (240.3695) Linear and nonlinear light scattering from surfaces; (290.1483) BSDF, BRDF, and BTDF; (190.5330) Photorefractive optics; (100.0118) Imaging ultrafast phenomena.
http://dx.doi.org/10.1364/AO.54.002141

1. Introduction

Vanadium dioxide is a promising photorefractive material for modern optoelectronics [1–4]. Upon heating, uniaxial stress, electron injection, or light illumination VO_2 undergoes a first-order insulator-to-metal phase transition (I-M PT) with considerable change of elastic, structural, electronic, and optical properties. The first observation of photoinduced PT in VO_2 was performed by Roach and Balberg [5]. While the thermally induced PT occurs at near room temperature $T_c = 341$ K [6], the light-induced transition is nonthermal and can be initiated on an ultrafast time scale at temperature significantly below T_c [7–9].

The light-induced PT dynamics of VO_2 is a complex process that involves many degrees of freedom. It depends on film morphology, strain, structural defects, external electric field, incident light polarization, wavelength, pulse duration, and intensity [10–16]. VO_2 nanoparticles and nanocrystalline films show size-dependent transition dynamics [17–20]. The ultrafast I-M PT of nanocrystalline films occurs within 130 fs at sufficiently high laser excitation, while, at lower excitation, the transition becomes much slower and takes tens of picoseconds. It was shown previously [21,22] that the slow component of PT within ~100–300 ps can be related to a competitive process between thermal relaxation and phonon interaction with cooperative photoexcited electronic states. The PT threshold can be decreased by introducing Au nanoparticles in a VO_2 matrix due to surface-plasmon-polariton field enhancement and

1559-128X/15/082141-10$15.00/0

hot-electron injection from Au to VO_2 [23,24]. Optical excitation can produce a metastable state [19,25], specific transient [7,12,15,26], or monoclinic metal-like state of VO_2 at high pressure [27]. Recent findings on ultrafast phonon dynamics [15] show that the laser excitation does not produce significant softening of phonon modes before the PT. Instead, the first-order PT occurs due to prompt change of the lattice potential.

Ultrafast light-induced PT is driven by nonequilibrium photoexcited electronic states, but the exact mechanism of the PT is still not fully understood. Several models have been proposed to explain this phenomenon. The general characteristics of phonon dynamics during PT were discussed by Cavalleri *et al.* [28], Kübler *et al.* [8], Semenov [29], Hada *et al.* [25], and recently by van Veenendaal [30] and Appavoo *et al.* [23]. These authors pointed out that photoexcited electrons can modify the vibrational spectrum of VO_2 and provide conditions for the PT. The main features of PT dynamics on different time scales can also be explained in terms of ultrafast charge-transfer and vibronic relaxation of photoexcited states [14,31].

The problem of understanding the thermal and light-induced PT of VO_2 is aggravated by numerous conflicting experimental data. In some cases, thermal and nonlinear optical properties vary significantly from sample to sample. To date, the most reliable data were obtained for single-crystal nanorods, nanobeams, and nanoplatelets. Along with single-crystal VO_2, the information about PT dynamics of epitaxial and polycrystalline VO_2 films is of special interest, since these films represent different stochastic or highly ordered model systems with different morphology and concentration of structural defects. It is expected that the interaction between carriers via vibronic phonon mode and carrier-induced screening of the on-site Coulomb interactions in VO_2 plays a significant role in PT [30–34], and these processes are strongly dependent on film structure. The role of electron–electron correlations and electron–phonon and electron–surface scattering in VO_2 grains of different sizes can be a crucial issue in PT and other relaxation processes. Therefore, special experimental methods are required in order to observe multiscale structural dynamics.

In this paper, an angle-resolved ultrafast elastic light scattering technique was applied to obtain information about power spectral density (PSD), fractal dimension, and autocorrelation function (ACF) of the VO_2 surface far from equilibrium. Precise calculation of ACF and partial reconstruction of PSD data was performed using the Gerchberg–Saxton algorithm [35,36]. The ultrafast angle-resolved light scattering experiment opens a new possibility for the detection of mesoscale phase transformation and reveals anisotropic grain-size-dependent behavior. It has been observed that the characteristic transition time τ for crystalline film depends on polarization of the laser pump and noticeably increases for grains with sizes $d < 530$ nm. Numerical analysis shows that the size-dependence and anisotropy of the absorption coefficient can be the main origins, which alter τ. The transient autocorrelation length (ACL) of the surface shows an abrupt rise only after a 270 fs delay with respect to the laser pump. A distinctive transient anisotropy of the scattering pattern appears as well after ~300 fs. This behavior is likely a consequence of the complex stepwise PT of VO_2.

2. Experimental Details

A. Measurements

Epitaxial 30 nm thick film of vanadium dioxide with high phase purity was grown by pulsed laser deposition technique on *r*-cut sapphire (Al_2O_3) substrate. The light-induced PT dynamics of VO_2 on the mesoscale was studied with the scatterometer equipped by a femtosecond Spectra-Physics laser system, as shown in Fig. 1. This system consists of Ti:sapphire oscillator and regenerative amplifier operating at wavelength $\lambda = 800$ nm. Generated laser pulses are compressed down to 130 fs and split by a beam splitter into pump and probe beams. The sample was mounted on the holder SH. The probe pulses were frequency-doubled by a 100 μm thick BBO crystal to the wavelength $\lambda = 400$ nm, while the wavelength of pump radiation was $\lambda = 800$ nm. The shorter probe wavelength allowed monitoring multiscale surface structures with spatial frequencies up to $f = 1/\lambda = 2.5\ \mu m^{-1}$. Incident light was linearly polarized by a Glan-type prisms GP and GP'. The polarization of pump pulse was controlled by half-wave plate $\lambda/2$ and GP, so the mutual orientation of electric field vectors of pump ($\vec{E}_w$) and probe ($\vec{E}_o$) pulses can be set parallel or orthogonal. In order to initiate the PT of VO_2 film, the pump pulse was focused to a spot size of 1.2 mm with average fluence of $W = 4.7\ mJ/cm^2$. The spot size of the probe pulse was less than 100 μm in order to ensure interrogation of only a uniformly excited region of the sample. Intensity I_0 of the probe beam was substantially reduced by a neutral density filter to eliminate any nonlinear interaction of this beam with the sample. Scattered light within

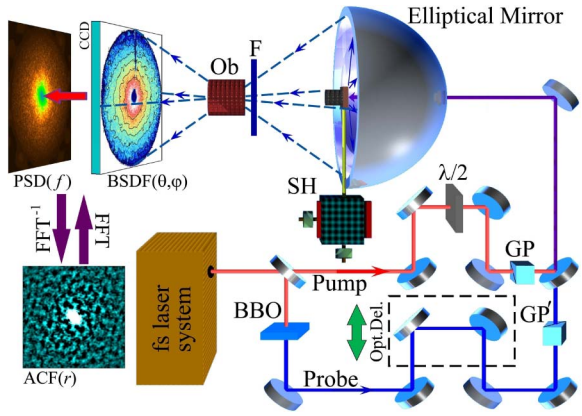

Fig. 1. Experimental setup for hemispherical angle-resolved light scattering measurements.

hemisphere was projected to a charge-coupled device (CCD) by elliptical mirror. This part of the optical setup was designed in accordance with the description given in [37]. A color filter F installed at the front of the objective Ob transmitted the probe light and blocked the leak of the pump radiation onto the CCD camera. The temporal delay t between pump and probe pulses was controlled by a motorized translation stage Opt. Del. equipped with a retroreflector.

Surface topography of the films was studied by atomic force microscope (AFM, Park Scientific Instruments, Autoprobe CP).

B. Scattering Data and Surface Statistics

The advantage of the angle-resolved light scattering technique is its ability to obtain statistical information about surface irregularities of different sizes [38–41], since each scattering angle corresponds to specific spatial frequency of the surface $f = 1/d = \sin\theta/\lambda$, where θ is the polar scattering angle and d is the characteristic size of irregularities. The scattering images were recorded by a SBIG CCD camera and stored in 765×510 pixel files. These data were used for calculation of the bidirectional scatter distribution function (BSDF), PSD function, and for reconstruction of ACF of the surface. These functions reflect general statistical properties of the surface. The BSDF can be directly calculated from angle-resolved light scattering as

$$\mathrm{BSDF}(\theta,\varphi) = \left(\frac{dI_{\mathrm{scatt}}(\theta,\varphi)}{d\Omega}\right)\frac{1}{I_0\cos\theta}, \tag{1}$$

where I_0 is the intensity of incident light, dI_{scatt} is the intensity of light scattered into solid angle $d\Omega$, and φ is the azimuthal angle. In this work, the BSDF indicatrices were obtained from experimental data with Eq. (1) and used for calculation of PSD of the surface roughness. The relation between BSDF measured at normal incidence and PSD is given as [41]

$$\mathrm{PSD}(f) = \frac{\lambda^4\,\mathrm{BSDF}(f)}{16\pi^2 Q\cos\theta}, \tag{2}$$

where Q is an optical factor that depends on light polarization, scattering angle, and dielectric constants. The Q-factor can be calculated using equations obtained by Elson [42–44]. The PSD function calculated from Eq. (2) represents the statistical distribution of surface roughness versus surface spatial frequency.

The information about correlation of surface irregularities can be obtained from the ACF

$$\mathrm{ACF}(r) = \lim_{L\to\infty}\frac{1}{L}\int_L z(r')z(r'+r)\mathrm{d}r', \tag{3}$$

where r is the translation length in the surface plane, and $z(r)$ is the surface profile defined over an area L. At zero translation, $\mathrm{ACF}(0) = \delta^2$, where δ is rms roughness [41]. In this work, we use the normalized autocorrelation functions $\mathrm{ACF}_s = \mathrm{ACF}/\delta^2$, calculated from scattering data.

The Wiener–Khinchin theorem shows that the ACF is a Fourier transform of PSD

$$\mathrm{ACF}(r) = \int_{-\infty}^{+\infty}\mathrm{PSD}(f)e^{i2\pi fr}\mathrm{d}f. \tag{4}$$

Despite this simple relation between ACF and PSD, the correct calculation of ACF from PSD can be significantly affected in practice by effective bandwidth limits with the absence of PSD data at low spatial frequencies blocked by the sample holder as well as above the frequency $f_{\max} = \sin 90°/\lambda = 1/\lambda$ [41,45,46]. In most cases, absence of experimental data introduces significant artifacts in ACF. Therefore, correct calculation of ACF requires reconstruction of PSD within regions where the experimental data are absent. One of the solutions is the extrapolation of PSD using an "ABC" model [46]. However, in the present work we apply the Gerchberg–Saxton error reduction (ER) algorithm [35,36], which produces a more natural precise reconstruction of the ACF and PSD pair.

The n-th cycle of the ER algorithm can be written as

$$\begin{aligned}
&\mathrm{ACF}_n^*(r) = \mathrm{FFT}^{-1}\{\mathrm{PSD}_n(f)\}\\
&\mathrm{ACF}_n(r) = \begin{cases}\mathrm{Re}[\mathrm{ACF}_n^*(r)] & \text{if } r\in S\\ 0 & \text{if } r\notin S\end{cases}\\
&\mathrm{PSD}_{n+1}^*(f) = \mathrm{FFT}\{\mathrm{ACF}_n(r)\}\\
&\mathrm{PSD}_{n+1}(f) = \begin{cases}\mathrm{PSD}_{\mathrm{obs}}(f) & \text{if } f\in f_{\mathrm{obs}}\\ \mathrm{Re}[\mathrm{PSD}_{n+1}^*(f)] & \text{if } f\notin f_{\mathrm{obs}},\\ & \mathrm{Re}[\mathrm{PSD}_{n+1}^*(f)]\ge 0\\ 0 & \text{otherwise}\end{cases}
\end{aligned} \tag{5}$$

where $\mathrm{PSD}_{\mathrm{obs}}$ is the measured PSD function within f_{obs} spatial frequencies, S is the ACF's support (i.e., area where ACF is nonzero), ACF^* is the inverse fast Fourier transform FFT^{-1} of the measured PSD with reconstructed part, and PSD^* is the direct fast Fourier transform FFT of the reconstructed ACF.

The constraints in the ER algorithm are quite strong, since both ACF and PSD functions are real; hence, the ACF phase is 0 or π. This provides reliable and relatively fast convergence to reproducible results. The progress of iterations was monitored with the real-space squared error

$$\mathcal{E}_n^2 = \frac{\sum_{r\notin S}|\mathrm{ACF}_n^*(r)|^2}{\sum_{r\in S}|\mathrm{ACF}_n^*(r)|^2}. \tag{6}$$

The size of the support S was chosen to be comparable with the size of probe beam so as to provide convergence with minimal $\mathcal{E}_n^2$. A detailed description of the ER algorithm and its application to phase reconstruction and imaging can be found in [36].

For the ACF computation, the combination of the ER with hybrid input–output (HIO) technique reduces algorithm stagnation. However, in most cases it was enough to apply only ER (5) in order to obtain robust satisfactory reconstruction of the ACF and PSD Fourier transform pair. We note that the ER with HIO algorithm can also be used to retrieve the full phase map of the light scattering field and reconstruct the surface profile from BSDF data.

3. Results and Discussion

A. Transient Light Scattering and Structural Dynamics

The ultrafast studies of light-induced PT were performed for the VO_2/Al_2O_3 film with thickness below the penetration depth of the pump pulse (56 nm for the semiconducting phase). Therefore, optical excitation was produced uniformly across the film. This allowed suppressing some artifacts in the measured signal related to strong absorption in VO_2. The AFM image of surface topography (Fig. 2) shows that the average size of VO_2 grains is $d \sim 250$ nm. Some grains are merged into larger structures with $d \gtrsim 500$ nm. The root-mean-square roughness of the surface calculated from AFM data is $\delta = 41$ Å. The r-cut Al_2O_3 substrate has a rectangular atomic lattice on the surface, and the VO_2 crystalline film is epitaxially oriented on this substrate with directions $[010]_{VO2} \| [100]_{Al2O3}$ and $[001]_{VO2} \| [02\bar{1}]_{Al2O3}$ [14,47,48]. This resulted in slight scattering anisotropy with respect to $[010]_{VO2}$ (b_m) and $[001]_{VO2}$ (c_m) directions [Fig. 3(a)].

The PSD function [Fig. 3(b)] for the VO_2 film in insulating phase was calculated using Elson equations for rough surface scattering [44]. The optical constants for these calculations were obtained from additional angular measurements of reflection coefficient and data fit for s and p polarization of the incident light. The cross section of scattering indicatrix at arbitrary direction shows that the BSDF for VO_2/Al_2O_3 is practically a scaled PSD function, as shown in Fig. 3(c). This indicates that the correct information about statistical redistribution of surface inhomogeneities can be obtained from BSDF data. This "scatter prediction" is valid for optically smooth surfaces with $\delta < \lambda/(4\pi)$, in accordance with the Rayleigh smooth-surface criterion [41]. The VO_2 film satisfies this requirement. Thus, qualitatively, the BSDF(f) is fairly close to PSD(f) function and weakly changes during the PT. We note that the information about surface statistics obtained from BSDF(f) becomes useful when the system is in a nonequilibrium state, and the material optical constants are unknown or undergo small alterations.

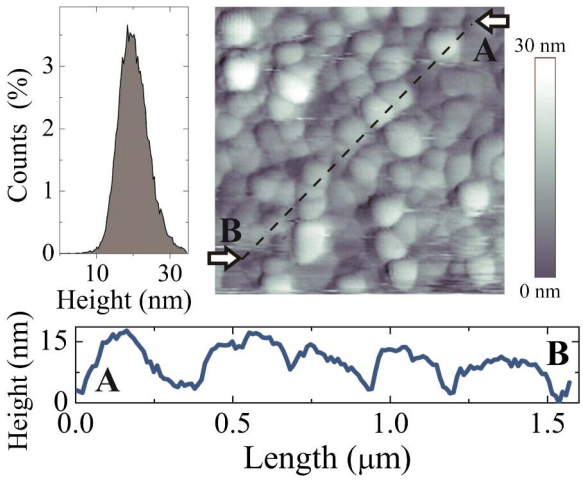

Fig. 2. AFM topography of VO_2 film. Right upper panel: 1.4 × 1.4 μm AFM image. Left upper panel: Surface height distribution histogram. Lower panel: Cross section of AFM image.

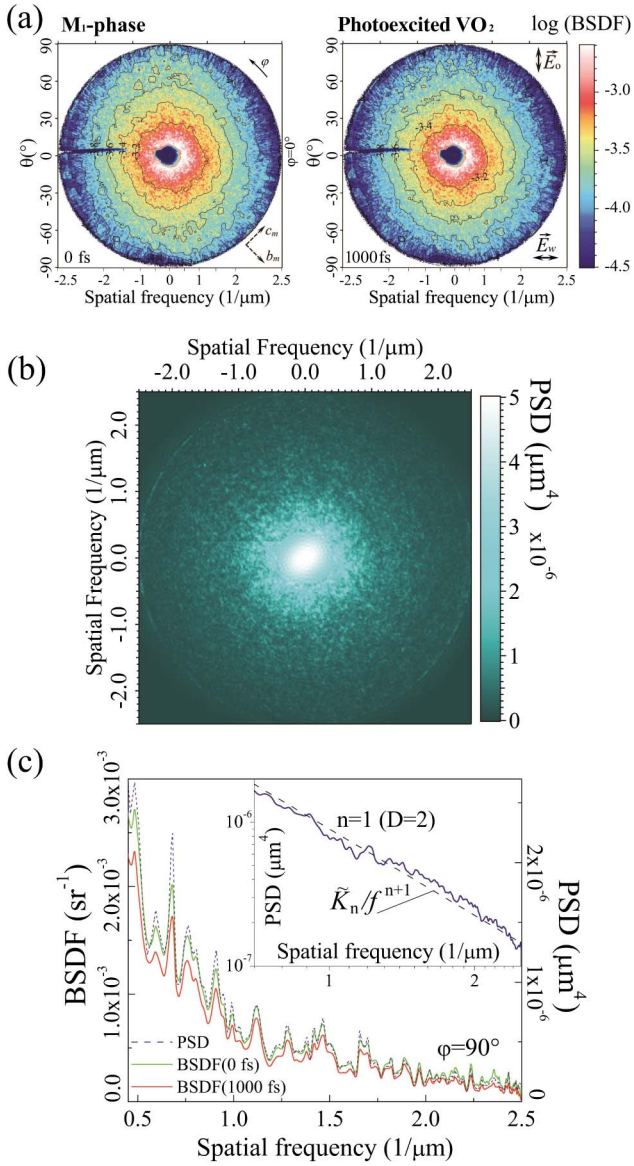

Fig. 3. (a) Ultrafast scattering (see Media 1); log(BSDF) indicatrices for insulating and photoexcited VO_2. (b) Power spectral density of the surface irregularities. Central region of PSD map blocked by the sample holder was reconstructed using the Gerchberg–Saxton ER algorithm. (c)PSD(f) and BSDF(f) cross sections at $\varphi = 90°$. Inset shows the azimuthally averaged PSD function.

The PSD(f) function in a log–log graph [inset in Fig. 3(c)] reveals its fractal-like linear behavior. Thus, the PSD(f) can be approximated by a 2D power spectrum as $\mathrm{PSD}(f) = \tilde{K}_n/f^{n+1}$, where the $\tilde{K}_n$ and n are fractal parameters [45,49]. The Hausdorff–Besicovitch dimension is defined as $D = (5-n)/2$. The parameters obtained for PSD of VO_2 film are $n = 1$ and $D = 2$, which correspond to the *extreme fractal* and indicate close-packed crystallites of a rugged surface [50].

Figure 3(c) shows decrease of BSDF signal with time. However, the position of all diffraction peaks in the scattering indicatrix remains the same within 1 ps. This fact is strong evidence that the surface geometry also remains the same. We note that the structural dynamics upon light-induced PT substantially differs from the case of thermal transition where the VO_2 film undergoes twinning and domain formation accompanied by a shift of diffraction peaks with noticeable transformation of total scattering indicatrix [48]. The sub-picosecond time scale is too short for long-range phonon interactions, which could result in twinning or reorientation of VO_2 microcrystallites. The total switching into metallic phase occurs simultaneously and independently in different domains of the film. Only short-range interactions are considerable on the observed 1 ps time scale. This PT mechanism does not imply nucleus growth in a metastable environment.

While the surface geometry of VO_2/Al_2O_3 film remains the same during the ultrafast PT, the lattice transformation from monoclinic M_1 to tetragonal R-phase changes the dielectric permittivity tensor. The alteration of dielectric constant $\Delta\varepsilon$ slightly changes the optical factor Q in Eq. (2) and, as a result, the BSDF scattering indicatrix. For epitaxial VO_2 film, the alteration of $\Delta\varepsilon$ and Q is anisotropic [14]. Moreover, if $\Delta\varepsilon$ depends on particle size, it qualitatively modifies the PSD function of the surface versus f.

The contribution of $\Delta\varepsilon$ to the scattering indicatrix was observed from the transient change $\Delta\mathrm{BSDF}(t)/\mathrm{BSDF}(0)$, where $\Delta\mathrm{BSDF}(t) = \mathrm{BSDF}(t) - \mathrm{BSDF}(0)$, for orthogonal [$\vec{E}_w \perp \vec{E}_o$, Fig. 4(a)] and parallel [$\vec{E}_w \| \vec{E}_o$, Fig. 4(b)] polarizations of pump and probe pulses. Indicatrices obtained for $\vec{E}_w \perp \vec{E}_o$ show some anisotropy, which can be assigned to the photoinduced anisotropy of the Q-factor. However, changing the polarization of the pump pulse to $\vec{E}_w \| \vec{E}_o$ results in slightly different distribution of $\Delta\mathrm{BSDF}(t)/\mathrm{BSDF}(0)$ with a higher level of isotropy. This result indicates that the polarization of pump pulse can be a critical parameter in PT dynamics. Independently on light polarization, a specific scattering pattern appears within $0° < \theta < 60°$. Thus, at $t > 600$ fs $\Delta\mathrm{BSDF}(t)/\mathrm{BSDF}(0) \approx -0.1$ in the central part of the indicatrix, but at $\theta > 60°$ it changes to slightly anisotropic pattern with $\Delta\mathrm{BSDF}(t)/\mathrm{BSDF}(0) \approx -0.3$.

As shown in Fig. 2, the average size of the largest VO_2 grains is $d \sim 250$ nm, which corresponds to $f = 4\ \mu\mathrm{m}^{-1}$. This spatial frequency is above the range attainable by the light scattering technique. On the other hand, some grains are merged into domains with $d \gtrsim 500$ nm, $f \lesssim 2\ \mu\mathrm{m}^{-1}$. Light scattering by these domains corresponds to $0° < \theta < 55°$ angular range, which is very close to the range where the specific scattering pattern in Fig. 4 was observed. Therefore, scattering within this angular rage is assigned to the light scattering by merged VO_2 grains.

The distinctive scattering pattern within $0° < \theta < 60°$ in Fig. 4 (see also Media 1) appears after ~300 fs due to grain-size-dependent structural PT. It is believed that the transient scattering signal at time $t \lesssim 300$ fs is related mostly to the nonlinear response of the electronic subsystem via third-order optical nonlinearity. However, the screening of Coulomb correlations due to photoexcitation of free carriers can result in subsequent bandgap renormalization with additional contribution to the first-order susceptibility on a ~300 fs time scale. The nature of such nonlinear dynamics requires additional studies.

We now turn our attention to the transient ACF of the surface. Optical constants of VO_2 in a photoexcited state were unknown; therefore, the calculation

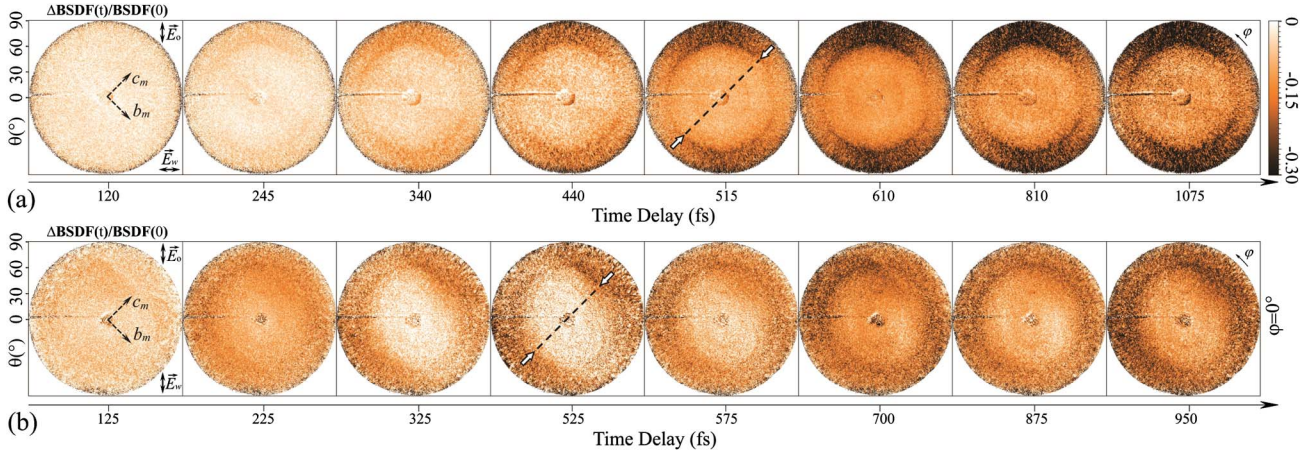

Fig. 4. Transient change $\Delta\mathrm{BSDF}(t)/\mathrm{BSDF}(0)$ of the scattering signal upon light-induced PT. (a) $\vec{E}_w \perp \vec{E}_o$. (b) $\vec{E}_w \| \vec{E}_o$. Arrows at $t = 515$ fs in (a) and at $t = 525$ fs in (b) mark central pattern of the indicatrix (see text for details).

of PSD was not performed for I-M PT. On the other hand, for optically smooth VO_2 film, the BSDF(f) is nearly a scaled PSD(f) function, as shown above [see Fig. 3(c)]. Therefore, we applied the "scatter prediction" approximation, where the experimentally measured BSDF(f) was used to describe the PSD of the surface. Thus, the surface ACF was calculated by Fourier transform of BSDF(f) data. Temporal evolution of ACF_s shows a relatively small change ΔACF_s [Figs. 5(a)–5(c)]. The ACF_s pattern during the light-induced PT remains almost the same. Such behavior is assigned to the transient evolution of VO_2 optical constants but without film twinning or modification of surface relief.

Structural PT produces a change of the dielectric permittivity tensor, increasing the optical isotropy

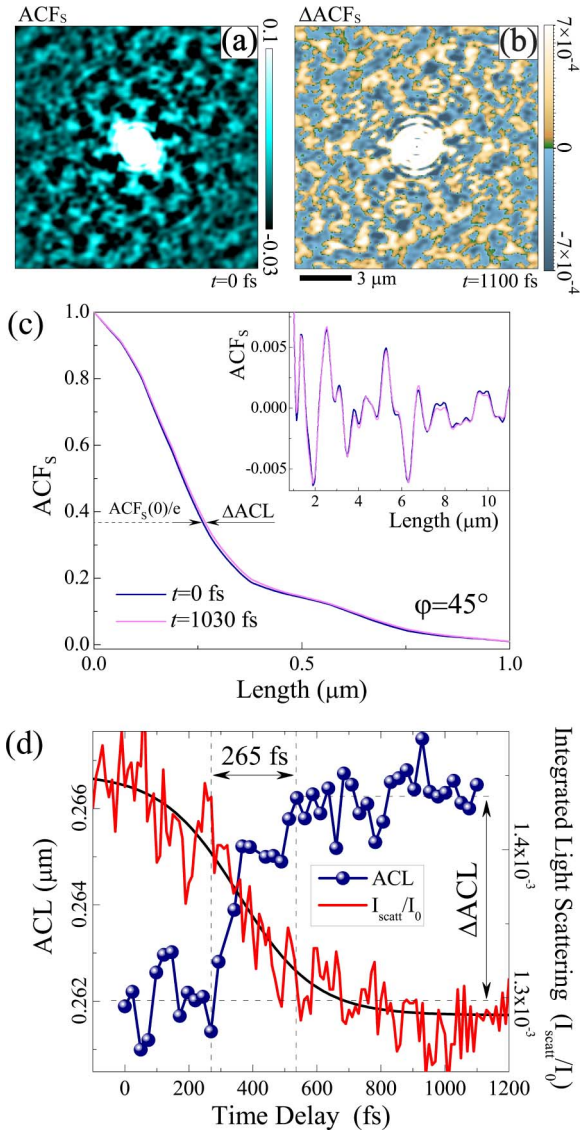

Fig. 5. (a) Autocorrelation function of the surface (see Media 1). (b) Change of ACF_s in photoexcited metallic state. (c) Cross section of ACF_s distribution at $\varphi = 45°$. (d) Transient autocorrelation length and light scattering signal integrated within hemisphere. Solid line is a sigmoidal fit.

of the film in the metallic R-phase [14]. As the film switches to metal, the symmetry of the VO_2 lattice increases, and the amplitude of *spatial oscillations* of ACF_s at $r > 1.0$ μm slightly diminishes, as seen in the Fig. 5(c) inset and the ΔACF_s map in Fig. 5(b). Moreover, the transient behavior of ΔACF_s also demonstrated some *temporal oscillations* (see Media 1) associated with modulation of VO_2 optical constants by photoexcited coherent lattice vibrations [8,15,27,51].

The transient change of the central maximum within $0 < r < 1.0$ μm shows slight but well-resolved distinctive broadening during the PT [Figs. 5(b) and 5(c)]. This maximum originates from statistically random distribution of surface irregularities and fluctuations of optical constants, and its broadening results in increase of the surface ACL within $\Delta ACL = 4.2 \times 10^{-3}$ μm [Fig. 5(d)]. Thus, the ACL increases abruptly after a 270 fs delay, during 265 fs, due to increasing optical isotropy and homogeneity of the film.

The evolution of ACL differs from that of the integrated light scattering signal I_{scatt}/I_0, where the signal changes immediately as the laser pump pulse excites the sample [Fig. 5(d)]. Such behavior of ACL can indicate a delay between the laser pump instant and a structural transformation of the VO_2 film. This result agrees with the transient dynamics of $\Delta BSDF(t)/BSDF(0)$ [Fig. 4] and with conclusions obtained in [15,48,52]. It is believed that the photo-induced screening of the Coulomb potential reduces the dimerization of V ions during the first ~300 fs and results in instability of the M_1 phase, with the subsequent stepwise structural transition. It is important to note that the 300 fs time scale is close to the characteristic time $\tau^* \simeq 120$ fs of the resonance phonon scattering on V-V dimers obtained in [19]. This phonon scattering can be one of the parameters that control the resonance vibronic transition from an optically excited state in the insulating M_1 phase to an unoccupied excited state of the metallic R-phase [31].

B. Phase Transition Rate of Mesoscale VO_2

The photoinduced PT is accompanied by abrupt decrease of the total scattering signal I_{scatt}/I_0 within 800 fs [Fig. 5(d)]. During this time, the film switches into a metallic state. However, Fig. 5(d) does not represent a dependence of τ on the size of VO_2 grains. The information about the size-dependent transition rate was obtained from the angular distribution of scattered light. In order to compare τ for structures with different spatial frequencies and to exclude possible artifacts related to the polarization of the *probe* pulse, the scattering intensity I^*_{scatt} was normalized and scaled between 0 and 1, with a unit value for insulating (at $t = 0$ fs) and zero value for the metallic phase (at $t = 1500$ fs) [Figs. 6 and 7(a)]. The normalized data is insensitive to the transient polarization anisotropy of the scattering indicatrix related to the change of the dielectric permittivity tensor and

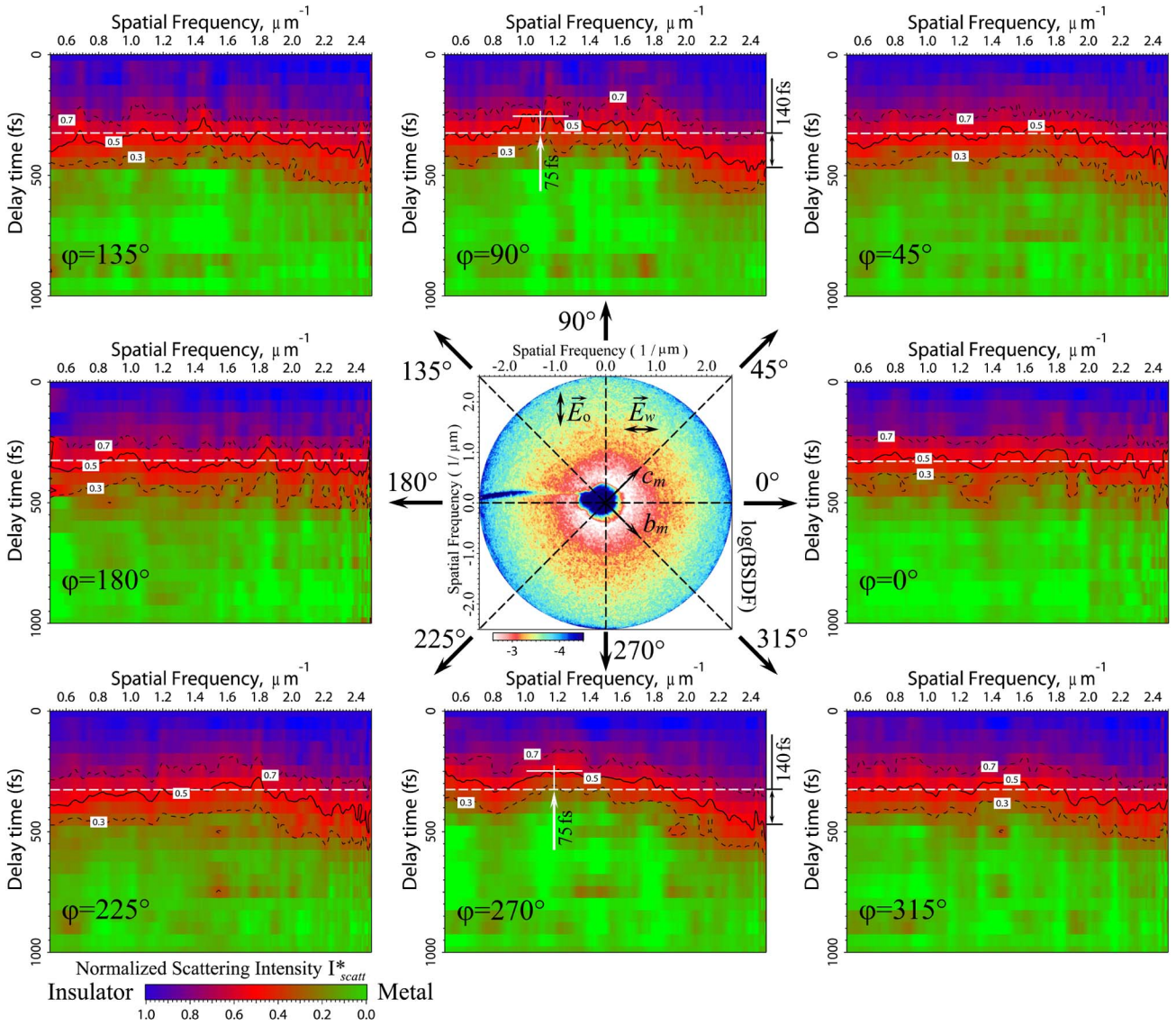

Fig. 6. Evolution of normalized scattering intensity for different spatial frequencies and azimuthal angles during light-induced phase transition (see Media 2). Central figure represents log(BSDF) indicatrix at $t = 0$ fs.

precisely represents the map of size-dependent evolution of the VO_2 phase. The PT time τ is defined here as $\tau = 2\tau_{\frac{1}{2}}$, where $\tau_{\frac{1}{2}}$ is the time for the signal to drop to 0.5 value.

As can be seen in Fig. 7(a), the transient scattering signal has an oscillatory component caused by the coherent lattice vibrations [8,15,27,51]. For different spatial frequencies, the period and phase of the oscillations slightly vary, indicating that the coherent phonon dynamics are likely affected by the size of VO_2 grains and local strain fields. As a result, a superposition of these oscillations suppresses a distinct oscillatory response in the signal of total integrated scattering [Fig. 5(d)].

Figure 6 shows that the PT rate depends on spatial frequency f and also on angle φ. At $\varphi = 0°$, 180°, the characteristic PT time $\tau = 2\tau_{\frac{1}{2}} = 650$ fs weakly varies, and $\tau_{\frac{1}{2}} = 325$ fs is marked in Fig. 6 by a dashed line. The strongest dependence of time τ on f is observed for VO_2 grains ordered along direction $\varphi = 90°$, 270°, where τ varies from $\tau = 500$ fs to $\tau = 930$ fs. This result constitutes the experimental evidence of size-dependent and anisotropic PT on a subpicosecond time scale for different VO_2 grains of the film. It is noted that the measurements were conducted at moderate laser excitation, above the PT threshold. In additional experiments, it was found that an increase in optical pump shifts the characteristic PT time toward the autocorrelation width of the laser pulse, below the resolution threshold of the optical setup. In this case, the grain-size dependence and azimuthal anisotropy of measured signal vanishes.

It has to be noted that the VO_2 grains with various τ values are ordered along the $\varphi = 90°$, 270° direction, transversely to the polarization of laser pump. Moreover, no noticeable correlation was found between τ and b_m or c_m directions of epitaxial film. These facts indicate that the anisotropy of τ depends

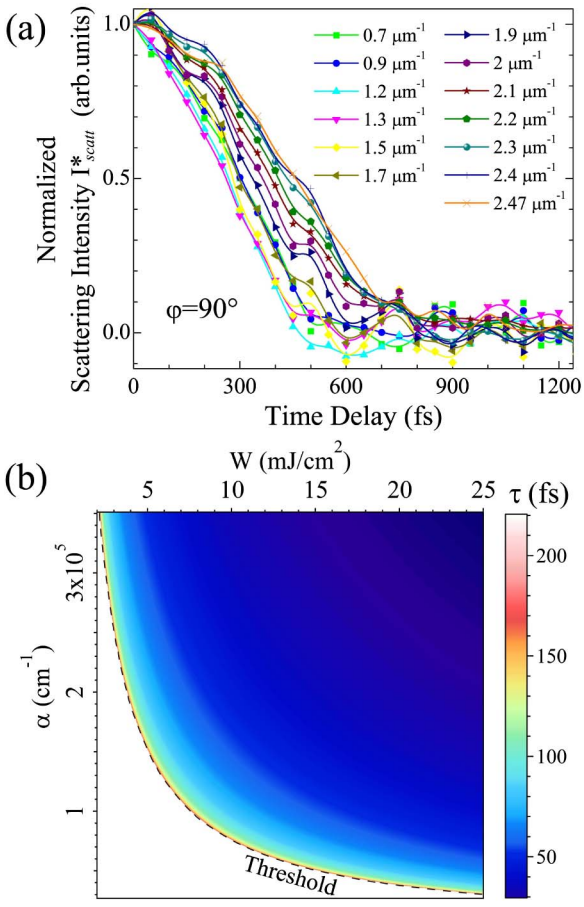

Fig. 7. (a) Photoinduced phase transition dynamics of VO_2 irregularities with different spatial frequencies at $\varphi = 90°$ (cross sections of the data mapped in Fig. 6). (b) Characteristic PT time calculated for 1.55 eV optical excitation.

rather on orientation and ordering of VO_2 grains with respect to polarization of the laser *pump* pulse.

The PT time depends on different parameters (i.e., laser pump pulse duration, fluence, wavelength, concentration of photoexcited carriers, nonstoichiometry, material density, bandgap, defects, electron–electron and electron–phonon scattering rate, etc.). A good estimation of τ is given by Semenov in his theoretical work [29] as

$$\tau = \sqrt{\frac{\pi m R^2}{32b}} \int_0^{\xi_0} \left[\frac{\pi\alpha(1-r_0)W}{2N\hbar\omega}(\xi_0-\xi) - \frac{\xi^2}{2}\ln\frac{\xi}{\xi_0} - \frac{\xi_0^2-\xi^2}{4} \right]^{-\frac{1}{2}} d\xi, \tag{7}$$

where N is the concentration of vanadium atoms, α is the absorption coefficient, r_0 is the reflection coefficient, W is the pump fluence, m is the mass of vanadium atom ($m \simeq 8.5 \times 10^{-23}$ g), R is the effective radius of electron wave function in $3d$-state ($R \approx 4.1 \times 10^{-9}$ cm), $\hbar\omega$ is the photon energy, $4b$ is the width of conduction d-band in metallic phase ($4b \approx 1.1$ eV), and ξ is the order parameter with $\xi_0 = 0.5$ [29]. The threshold fluence W_c required to initiate the structural PT can be derived from Eq. (7) as

$$W_c \simeq \frac{0.53\xi_0 N\hbar\omega}{\pi\alpha(1-r_0)}. \tag{8}$$

In order to calculate W_c, the absorption coefficient $\alpha = 1.8 \times 10^5$ cm^{-1} was obtained from transmission measurements for $\lambda = 800$ nm. The reflection coefficient was found as $r_0 = 0.18$. Using photon energy $\hbar\omega = 1.55$ eV and $N = 3 \times 10^{22}$ cm^{-3} [53], the threshold fluence obtained with Eq. (8) is $W_c = 4.3$ mJ/cm^2. This value is very close to the experimentally observed one in [7–9,52,54].

To support the discussion of experimental data and to provide further insight into PT dynamics, we have performed numerical calculation of τ with Eq. (7) versus α and W, assuming all other parameters are held constant. Figure 7(b) shows significant dependence of time τ on α and W, when laser excitation approaches the PT threshold. The calculated time τ is found to be smaller than the experimentally observed values. Nevertheless, Fig. 7(b) shows a fairly reasonable estimation of τ and allows understanding of the general dependence of time τ on laser fluence and on optical absorption, which is related to the crystallinity of the film.

Figure 7(b) indicates that, if α depends on the size of VO_2 grains, the time τ will also show grain-size dependence. Assuming that the ultrafast PT occurs due to photoexcitation of free carriers, the variation in α will result in changes in the concentration of the carriers, affecting τ. Optical birefringence of the epitaxial VO_2/Al_2O_3 film provides anisotropy of α. Moreover, the absorption cross section depends on shape and orientation of particles with respect to light polarization [55], which probably is the main origin of τ anisotropy on the mesoscale. It is believed that the size-dependent PT rate is also enhanced by misfit strain in thin VO_2 films, since this strain can change the birefringence of the film and α.

Figures 6 and 7(a) show that, at $\varphi = 90°, 270°$, the time $\tau_{\frac{1}{2}}$ shifts to its minimal value $\tau_{\frac{1}{2}} = 250$ fs for VO_2 structures with $f = 1.0$–1.8 μm^{-1}, but, above $f = 1.9$ μm^{-1}, it gradually increases up to $\tau_{\frac{1}{2}} = 465$ fs, shifting from its average level ($\tau_{\frac{1}{2}} = 325$ fs). Taking into account data in Fig. 7(b), VO_2 grains with $f > 1.9$ μm^{-1} ($d < 530$ nm) should have a lower absorption coefficient and, therefore, longer PT time.

4. Conclusion

In this paper, photoinduced insulator-to-metal phase transition and ultrafast scattering dynamics have been discussed. We show that the Gerchberg–Saxton algorithm can be applied for accurate calculation of a surface autocorrelation function (ACF) from angle-resolved scattering data and for partial reconstruction of PSD function. Upon light-induced PT, the general patterns of the scattering indicatrix and ACF show relatively small change, since the surface geometry remains the same. Grain reorientation or film twinning was not detected on the subpicosecond time scale. However, ultrafast transformation of the dielectric permittivity tensor during first-order

PT results in a specific pattern of the scattering indicatrix $\Delta\mathrm{BSDF}(t)/\mathrm{BSDF}(0)$ within $0° < \theta < 60°$. This transient pattern is assigned to different structural dynamics in grains of different size, and it emerges only after a ~300 fs delay. The ACL of the surface abruptly increases after 270 fs. This behavior is presumably a signature of stepwise PT dynamics, where the lattice transformation process is separated by several tens or hundreds of femtoseconds from the laser pump instant.

Ultrafast elastic light scattering by epitaxial VO_2/Al_2O_3 film also reveals anisotropy of the characteristic PT time τ. It noticeably increases from $\tau = 650$ fs to $\tau = 930$ fs for grains with sizes $d < 530$ nm and depends on orientation of VO_2 grains with respect to the polarization direction of the laser pump. Numerical analysis shows that τ is likely altered by size-dependence and anisotropy of the VO_2 absorption coefficient.

The authors gratefully acknowledge support from the UPRM College of Arts and Sciences. N. S. was supported in part by the National Science Foundation under grant ECCS-1139773.

References

1. Z. Yang, C. Ko, and S. Ramanathan, "Oxide electronics utilizing ultrafast metal-insulator transitions," Annu. Rev. Mater. Res. **41**, 337–367 (2011).
2. J. D. Ryckman, K. A. Hallman, R. E. Marvel, R. F. Haglund, and S. M. Weiss, "Ultra-compact silicon photonic devices reconfigured by an optically induced semiconductor-to-metal transition," Opt. Express **21**, 10753–10763 (2013).
3. M. J. Dicken, K. Aydin, I. M. Pryce, L. A. Sweatlock, E. M. Boyd, S. Walavalkar, J. Ma, and H. A. Atwater, "Frequency tunable near-infrared metamaterials based on VO_2 phase transition," Opt. Express **17**, 18330–18339 (2009).
4. H. Coy, R. Cabrera, N. Sepúlveda, and F. E. Fernández, "Optoelectronic and all-optical multiple memory states in vanadium dioxide," J. Appl. Phys. **108**, 113115 (2010).
5. W. Roach and I. Balberg, "Optical induction and detection of fast phase transition in VO_2," Solid State Commun. **9**, 551–555 (1971).
6. F. J. Morin, "Oxides which show a metal-to-insulator transition at the Neel temperature," Phys. Rev. Lett. **3**, 34–36 (1959).
7. T. L. Cocker, L. V. Titova, S. Fourmaux, G. Holloway, H.-C. Bandulet, D. Brassard, J.-C. Kieffer, M. A. El Khakani, and F. A. Hegmann, "Phase diagram of the ultrafast photoinduced insulator-metal transition in vanadium dioxide," Phys. Rev. B **85**, 155120 (2012).
8. C. Kübler, H. Ehrke, R. Huber, R. Lopez, A. Halabica, R. F. Haglund, and A. Leitenstorfer, "Coherent structural dynamics and electronic correlations during an ultrafast insulator-to-metal phase transition in VO_2," Phys. Rev. Lett. **99**, 116401 (2007).
9. A. Pashkin, C. Kübler, H. Ehrke, R. Lopez, A. Halabica, R. F. Haglund, R. Huber, and A. Leitenstorfer, "Ultrafast insulator-metal phase transition in VO_2 studied by multiterahertz spectroscopy," Phys. Rev. B **83**, 195120 (2011).
10. A. Cavalleri, T. Dekorsy, H. H. W. Chong, J. C. Kieffer, and R. W. Schoenlein, "Evidence for a structurally-driven insulator-to-metal transition in VO_2: a view from the ultrafast timescale," Phys. Rev. B **70**, 161102 (2004).
11. M. Hada, D. Zhang, A. Casandruc, R. J. D. Miller, Y. Hontani, J. Matsuo, R. E. Marvel, and R. F. Haglund, "Hot electron injection driven phase transitions," Phys. Rev. B **86**, 134101 (2012).
12. H. Wen, L. Guo, E. Barnes, J. H. Lee, D. A. Walko, R. D. Schaller, J. A. Moyer, R. Misra, Y. Li, E. M. Dufresne, D. G. Schlom, V. Gopalan, and J. W. Freeland, "Structural and electronic recovery pathways of a photoexcited ultrathin VO_2 film," Phys. Rev. B **88**, 165424 (2013).
13. M. Liu, M. Wagner, J. Zhang, A. McLeod, S. Kittiwatanakul, Z. Fei, E. Abreu, M. Goldflam, A. J. Sternbach, S. Dai, K. G. West, J. Lu, S. A. Wolf, R. D. Averitt, and D. N. Basov, "Symmetry breaking and geometric confinement in VO_2: Results from a three-dimensional infrared nano-imaging," Appl. Phys. Lett. **104**, 121905 (2014).
14. S. Lysenko, V. Vikhnin, F. Fernandez, A. Rua, and H. Liu, "Photoinduced insulator-to-metal phase transition in VO_2 crystalline films and model of dielectric susceptibility," Phys. Rev. B **75**, 075109 (2007).
15. S. Wall, L. Foglia, D. Wegkamp, K. Appavoo, J. Nag, R. F. Haglund, J. Stähler, and M. Wolf, "Tracking the evolution of electronic and structural properties of VO_2 during the ultrafast photoinduced insulator-metal transition," Phys. Rev. B **87**, 115126 (2013).
16. C. Chen, Y. Zhao, X. Pan, V. Kuryatkov, A. Bernussi, M. Holtz, and Z. Fan, "Influence of defects on structural and electrical properties of VO_2 thin films," J. Appl. Phys. **110**, 023707 (2011).
17. R. Lopez, T. E. Haynes, L. A. Boatner, L. C. Feldman, and R. F. Haglund, "Size effects in the structural phase transition of VO_2 nanoparticles," Phys. Rev. B **65**, 224113 (2002).
18. M. Rini, A. Cavalleri, R. W. Schoenlein, R. López, L. C. Feldman, R. F. Haglund, L. A. Boatner, and T. E. Haynes, "Photoinduced phase transition in VO_2 nanocrystals: ultrafast control of surface-plasmon resonance," Opt. Lett. **30**, 558–560 (2005).
19. S. Lysenko, V. Vikhnin, A. Rúa, F. Fernández, and H. Liu, "Critical behavior and size effects in light-induced transition of nanostructured VO_2 films," Phys. Rev. B **82**, 205425 (2010).
20. H. Liu, O.-H. Kwon, J. Tang, and A. H. Zewail, "4D imaging and diffraction dynamics of single-particle phase transition in heterogeneous ensembles," Nano Lett. **14**, 946–954 (2014).
21. S. Lysenko, V. Vikhnin, G. Zhang, A. Rua, F. Fernandez, and H. Liu, "Insulator-to-metal phase transformation of VO_2 films upon femtosecond laser excitation," J. Electron. Mater. **35**, 1866–1872 (2006).
22. S. Lysenko, A. Rúa, V. Vikhnin, F. Fernández, and H. Liu, "Insulator-to-metal phase transition and recovery processes in VO_2 thin films after femtosecond laser excitation," Phys. Rev. B **76**, 035104 (2007).
23. K. Appavoo, B. Wang, N. F. Brady, M. Seo, J. Nag, R. P. Prasankumar, D. J. Hilton, S. T. Pantelides, and R. F. Haglund, "Ultrafast phase transition via catastrophic phonon collapse driven by plasmonic hot-electron injection," Nano Lett. **14**, 1127–1133 (2014).
24. D. W. Ferrara, E. R. MacQuarrie, J. Nag, A. B. Kaye, and R. F. Haglund, Jr., "Plasmon-enhanced low-intensity laser switching of gold::vanadium dioxide nanocomposites," J. Appl. Phys. **98**, 241112 (2011).
25. M. Hada, K. Okimura, and J. Matsuo, "Photo-induced lattice softening of excited-state VO_2," Appl. Phys. Lett. **99**, 051903 (2011).
26. R. Yoshida, T. Yamamoto, Y. Ishida, H. Nagao, T. Otsuka, K. Saeki, Y. Muraoka, R. Eguchi, K. Ishizaka, T. Kiss, S. Watanabe, T. Kanai, J. Itatani, and S. Shin, "Ultrafast photoinduced transition of an insulating VO_2 thin film into a nonrutile metallic state," Phys. Rev. B **89**, 205114 (2014).
27. W.-P. Hsieh, M. Trigo, D. A. Reis, G. Andrea Artioli, L. Malavasi, and W. L. Mao, "Evidence for photo-induced monoclinic metallic VO_2 under high pressure," Appl. Phys. Lett. **104**, 021917 (2014).
28. A. Cavalleri, C. Tóth, C. W. Siders, J. A. Squier, F. Ráksi, P. Forget, and J. C. Kieffer, "Femtosecond structural dynamics in VO_2 during an ultrafast solid-solid phase transition," Phys. Rev. Lett. **87**, 237401 (2001).
29. A. Semenov, "Time of a semiconductor-metal phase transition induced by an ultrashort light pulse in vanadium dioxide," Phys. Solid State **49**, 1157–1160 (2007).
30. M. van Veenendaal, "Ultrafast photoinduced insulator-to-metal transitions in vanadium dioxide," Phys. Rev. B **87**, 235118 (2013).

31. V. Vikhnin, S. Lysenko, A. Rua, F. Fernandez, and H. Liu, "The model of ultrafast light-induced insulator-metal phase transition in VO_2," Solid State Commun. **137**, 615–620 (2006).
32. S. Biermann, A. Poteryaev, A. I. Lichtenstein, and A. Georges, "Dynamical singlets and correlation-assisted peierls transition in VO_2," Phys. Rev. Lett. **94**, 026404 (2005).
33. M. Gatti, F. Bruneval, V. Olevano, and L. Reining, "Understanding correlations in vanadium dioxide from first principles," Phys. Rev. Lett. **99**, 266402 (2007).
34. V. Eyert, "VO_2: A novel view from band theory," Phys. Rev. Lett. **107**, 016401 (2011).
35. R. W. Gerchberg and W. O. Saxton, "A practical algorithm for the determination of the phase from image and diffraction plane pictures," Optik **35**, 237–246 (1972).
36. J. R. Fienup, "Phase retrieval algorithms: a comparison," Appl. Opt. **21**, 2758–2769 (1982).
37. V. Sterligov and P. Cheyssac, "Apparatus and method for optical object characterization," French patent 0115232 (23 November 2001).
38. M. Zerrad, M. Lequime, and C. Amra, "Spatially resolved surface topography retrieved from far-field intensity scattering measurements," Appl. Opt. **53**, A297–A304 (2014).
39. S. Schröder, A. Duparré, L. Coriand, A. Tünnermann, D. H. Penalver, and J. E. Harvey, "Modeling of light scattering in different regimes of surface roughness," Opt. Express **19**, 9820–9835 (2011).
40. T. Herffurth, S. Schröder, M. Trost, A. Duparré, and A. Tünnermann, "Comprehensive nanostructure and defect analysis using a simple 3D light-scatter sensor," Appl. Opt. **52**, 3279–3287 (2013).
41. J. C. Stover, *Optical Scattering: Measurements and Analysis* (SPIE Optical Engineering, 1995).
42. J. M. Elson, "Light scattering from semi-infinite media for non-normal incidence," Phys. Rev. B **12**, 2541–2542 (1975).
43. J. M. Elson, "Theory of light scattering from a rough surface with an inhomogeneous dielectric permittivity," Phys. Rev. B **30**, 5460–5480 (1984).
44. J. M. Elson, "Characteristics of far-field scattering by means of surface roughness and variations in subsurface permittivity," Waves Random Media **7**, 303–317 (1997).
45. E. L. Church, "Fractal surface finish," Appl. Opt. **27**, 1518–1526 (1988).
46. S. Lysenko, B. Snopok, V. Sterligov, and Y. Shirshov, "Statistical properties of surfaces: features of the calculation of the autocovariance function from the scattering indicatrix," Opt. Spectrosc. **91**, 801–809 (2001).
47. M. Borek, F. Qian, V. Nagabushnam, and R. K. Singh, "Pulsed laser deposition of oriented VO_2 thin films on r-cut sapphire substrates," Appl. Phys. Lett. **63**, 3288–3290 (1993).
48. S. Lysenko, F. Fernandez, A. Rua, and H. Liu, "Ultrafast light scattering imaging of multi-scale transition dynamics in vanadium dioxide," J. Appl. Phys. **114**, 153514 (2013).
49. M. V. Berry, "Diffractals," J. Phys. A **12**, 781 (1979).
50. M. V. Berry and Z. V. Lewis, "On the Weierstrass-Mandelbrot fractal function," Proc. R. Soc. London, Ser. A **370**, 459–484 (1980).
51. H.-T. Kim, Y. W. Lee, B.-J. Kim, B.-G. Chae, S. J. Yun, K.-Y. Kang, K.-J. Han, K.-J. Yee, and Y.-S. Lim, "Monoclinic and correlated metal phase in VO_2 as evidence of the Mott transition: coherent phonon analysis," Phys. Rev. Lett. **97**, 266401 (2006).
52. P. Baum, D.-S. Yang, and A. H. Zewail, "4D visualization of transitional structures in phase transformations by electron diffraction," Science **318**, 788–792 (2007).
53. C. N. Berglund and H. J. Guggenheim, "Electronic properties of VO_2 near the semiconductor-metal transition," Phys. Rev. **185**, 1022–1033 (1969).
54. D. Hilton, R. Prasankumar, S. Fourmaux, A. Cavalleri, D. Brassard, M. El Khakani, J. Kieffer, A. Taylor, and R. Averitt, "Enhanced photosusceptibility near T_c for the light-induced insulator-to-metal phase transition in vanadium dioxide," Phys. Rev. Lett. **99**, 226401 (2007).
55. C. F. Bohren and D. R. Huffman, *Absorption and Scattering of Light by Small Particles* (Wiley, 2008).